SENSORS

Guiding the design of superresolution tactile skins with taxel value isolines theory

Huanbo Sun* and Georg Martius*

Tactile feedback is essential to make robots more agile and effective in unstructured environments. However, high-resolution tactile skins are not widely available; this is due to the large size of robust sensing units and because many units typically lead to fragility in wiring and to high costs. One route toward high-resolution and robust tactile skins involves the embedding of a few sensor units (taxels) into a flexible surface material and the use of signal processing to achieve sensing with superresolution accuracy. Here, we propose a theory for geometric superresolution to guide the development of tactile sensors of this kind and link it to machine learning techniques for signal processing. This theory is based on sensor isolines and allows us to compute the possible force sensitivity and accuracy in contact position and force magnitude as a spatial quantity before building a sensor. We evaluate the influence of different factors, such as elastic properties of the material, structure design, and transduction methods, using finite element simulations and by implementing real sensors. We empirically determine sensor isolines and validate the theory in two custom-built sensors with 1D and 2D measurement surfaces that use barometric units. Using machine learning methods to infer contact information, our sensors obtain an average superresolution factor of over 100 and 1200, respectively. Our theory can guide future tactile sensor designs and inform various design choices.

INTRODUCTION

Tactile skins are indispensable in robotic applications to enable robots to perceive when, where, and how their bodies interactively contact other things (*1*–*6*). A common theme for surface tactile sensors is to integrate many small sensing units, forming a type of grid along a flat or curved surface. Each sensing unit, named a taxel, is responsible for sensing interactions near its location. For typical applications, a resolution is desirable that would imply numerous taxels (*4*, *5*, *7*–*11*); this is true both for small surface sensing, e.g., at the fingertips, and for large surfaces, e.g., around limbs. For fingertips, focused areas need a high density of small taxels to perceive high-resolution tactile information, which is similar to touch screens. For limbs, although tactile information is coarsely needed, taking the density distribution of human mechanoreceptors (*12*) as a reference requires still a large number of taxels. Technical challenges arise concerning the physical size of the taxels as well as growing manufacturing and wiring costs (*13*).

Many proposed tactile sensor designs are able to quantify contact across the sensing surface. They typically rely on resistive (*14*, *15*), capacitive (*16*–*18*), optoresistive (*19*, *20*), ferroelectric (*21*), or triboelectric (*22*) transduction methods. A common setting is a grid of taxels and a physical resolution matching the taxel density. A high density of smaller taxels and thinner wires are favorable to obtain a high resolution but less ideal due to mechanical fragility, electromagnetic noise, and cross-talk between taxels (*6*, *13*). In addition, vision-based tactile sensors (*23*–*28*) have demonstrated a new branch of solutions for high-resolution sensing, typically using an internal camera that views the soft contact surface from within. They can gain high spatial resolution with densely placed receptors at a potential cost of speed, power consumption, and computation.

Naturally, efforts are also made to acquire as much tactile information as possible from only a few physical taxels (*29*–*35*). The reduction of the number of taxels is generally possible because a taxel can monitor an extended patch on the surface, and multiple taxels can jointly provide information about tactile information at a certain position. The particular material properties lead to a characteristic spread of contact information to the sensing taxels. Different physical effects can be used, such as geometric and mechanical properties (*30*–*32*), electrical resistance (*33*, *34*), magnetic flux (*35*), heat flow and fluid dynamics (*36*), and so forth. The central idea is to solve the inverse problem of inferring tactile information from a few sensors, effectively creating high-resolution virtual taxels. This concept is also referred to as superresolution (SR) sensing (*37*, *38*). SR sensing assumes a subset of all possible stimulation patterns to occur, for instance, a few simultaneous touch points.

SR sensing was investigated in different areas, such as geostatistics (temperature and precipitation prediction) (*36*, *39*), material release detection (aerosol/chemical plume release) (*40*, *41*), and imaging systems (SR microscopy) (*37*, *42*). The used methods typically rely on the continuity and neighboring effects in the transmission medium and on solving inverse problems (signal processing) to reconstruct spatial information from a few sensors in a sparse configuration. Visual SR technologies have been studied for decades and achieved fundamental advancements in imaging systems that transcend the resolution limit (geometric SR) (*43*) and diffraction limit (optical SR) (*37*, *43*). In general, SR requires a restricted set of possible stimulation patterns. When considering the perception of lines, for instance, the human brain can judge edge alignment up to $^{1}/_{10}$th of the anatomical spacing of the mosaic of receptors in the retina (*44*, *45*)—a phenomenon known as hyperacuity. In comparison, the study of tactile SR in robotics is in its infancy.

Several tactile sensor designs achieve SR sensing, relying on geometric SR. A detailed comparison of these sensors is shown in Table 1. Lepora *et al.* (*30*) developed a Bayesian perception method to localize contact for a capacitive tactile sensor with 12 taxels and achieved a 35-fold SR. A 40-fold SR was achieved by a vision-based

Autonomous Learning Group, Max Planck Institute for Intelligent Systems, Tübingen, Germany.
*Corresponding author. Email: huanbo.sun (H.S.); georg.martius@tuebingen.mpg.de (G.M.)

Table 1. A comparison of state-of-the-art SR tactile sensors and our theory and design. For the developed prototypes in this article, we report both the prediction of our theory and the performance of the ML inference solution for the 1D case. The sign ~ indicates our calculation that approximates missing numbers in the literature. RMSE, root mean square error; MAE, mean absolute error; Smpl., simple form of Ω using the reported RMSE; Avg., averaging the force-specific Ω_k over the entire force range of 0.02 to 1.5 N, where *k* indicates the *k*th force intervals (0.01 N).

Sensor name	Transduction method	Surface shape	Evaluation length/area	No. of real taxels	Spacing *D* (mm)	Data processing	Output format	Localization RMSE (mm)	SR factor*		SR factor†	
									Smpl.	Avg.	Smpl.	Avg.
Lepora *et al.* (*30*)	Capacitive	2.5D	~433 (mm^2)	12	4	Bayesian perception	P	0.12‡ (MAE)	35	–	~798	–
TacTip (*46*)	Cam + Marker	3D	~2,513 (mm^2)	532	4	Bayesian perception	P	0.1‡ (MAE)	40	–	~150	–
Piacenza *et al.* (*47*)	Barometer (*48*)	2.5D	1,300 (mm^2)	5	~15	Ridge regression	P	1.6 (MAE)	~9	–	~32	–
HapDefX (*32*)	Resistive	3D	24,000 (mm^2)	10	~54	MLP	(P, F)	3.0	~18	–	~85	–
Piacenza *et al.* (*19*)	Optical	3D	~6,107 (mm^2)	30	~24	MLP	(P, F)	0.6‡ (MAE)	~40	32	~180	123
Hellebrekers *et al.* (*49*)	Magnetic	2D	1,600 (mm^2)	5 (3-axis)	15	MLP	(P, F)	0.86 (MAE)	~17	–	~138	–
Yan *et al.* (*35*)	Magnetic	2D	324 (mm^2)	9 (3-axis)	6	Analytic + MLP + Table	(P, F)	0.1 (MAE)	60	–	~1,146	–
Our theory in 1D	Barometer	1D	32.5 (mm)	6	6.5	Numeric	(P, F)	0.0525 + 0.0075	108	448	45	187
Our ML in 1D	Barometer	1D	32.5 (mm)	6	6.5	MLP	(P, F)	0.0416	156	254	65	106
Our ML in 2D	Barometer	2D	676 (mm^2)	25	6.5	MLP $_{(x, y)}$	(P, F)	0.1606	40	52	334	1,260

*Uses Ω = *D*/RMSE to calculate the SR factor. †Uses Ω = Length/(2 * *n* * RMSE) for 1D and Ω = Area/(*n* * π * $RMSE_x$ * $RMSE_y$) (Eq. 10) for 2D to calculate the SR factor. ‡Best reported performance.

tactile sensor (TacTip) by tracking moveable markers with the same method (*46*). Piacenza *et al.* (*47*) made a dome-shaped sensor by molding five TakkTile (*48*) pressure sensors under a rubber urethane layer and applied ridge regression to achieve a ninefold SR. HapDefX (*32*) used the spreading behavior of mechanical deformation by attaching a few strain gauges on a sizeable robotic limb shell and built a machine learning (ML) model with a structure of a multilayer perceptron (MLP) to achieve an 18-fold SR. Piacenza *et al.* (*19*) built a soft optic sensor that integrates 30 photodiodes to detect light emitted from 32 paired light-emitting diodes. An MLP model was trained to obtain a 40-fold SR. Hellebrekers *et al.* (*49*) embedded five magnetometers underneath a soft magnetic skin and trained an MLP model to achieve a 17-fold SR. Similarly, Yan *et al.* (*35*) used Hall sensors in a sparse configuration to detect the deformation of a magnetized flexible film and developed MLP models to achieve a 60-fold SR.

These sensors rely on the empirical knowledge that overlapping multiple taxels' perception fields triggers SR behavior. The design of well-performing sensors is typically achieved by an iterative optimization of all the involved components, namely, the mechanical design, data collection, and data processing steps (either analytical or data-driven). This process is naturally time-consuming, and it is nontrivial to identify bottlenecks preventing higher performances, especially when optimizing intermediate steps separately. To guide the design, a sound quantitative theory is desirable, which allows making informed decisions at all levels.

This article aims to provide such a theory by assessing the interplay of the involved physical components and information processing steps at a fundamental level. We want to predict achievable sensing performance depending on the involved design choices of the sensing mechanism, the material properties, and the data processing before building the sensor. We are particularly interested in understanding how ML methods can be related to the theory and used for inference.

Our proposed theory allows us to infer spatially resolved properties, such as accuracy and sensitivity for single contact, based on a single characteristic of the material-taxel interplay: taxel value isolines (TVIs). We demonstrate the application of the theory by designing two custom-built sensors that yield high SR sensing capabilities. In addition, we provide guidance for three common physical sensor types.

The model we use is a sensor comprising discrete taxels sparsely distributed in a continuous transmission medium underneath a sensing surface, as shown in Fig. 1. For sensing devices that can be described by this model, we derive the single-contact accuracy for position and force magnitude inference based on the TVIs; determine the minimal force profile for which localization is possible; provide conditions for simultaneous contacts to be distinguishable; evaluate the influence of different factors, such as elastic properties of the material, structure design, and transduction methods as well as contacting object shapes; and design a one-dimensional (1D) sensor and a 2D sensor using barometers to validate our proposed SR theory.

RESULTS

The model

We consider a class of tactile sensing devices intended for measuring force interactions on an extended surface that have an elastic transmission medium covering or embedding physical sensor units (taxels). A 1D model is shown in Fig. 1A(i). For a point contact, a single taxel value *s* is a function of the applied contact force strength

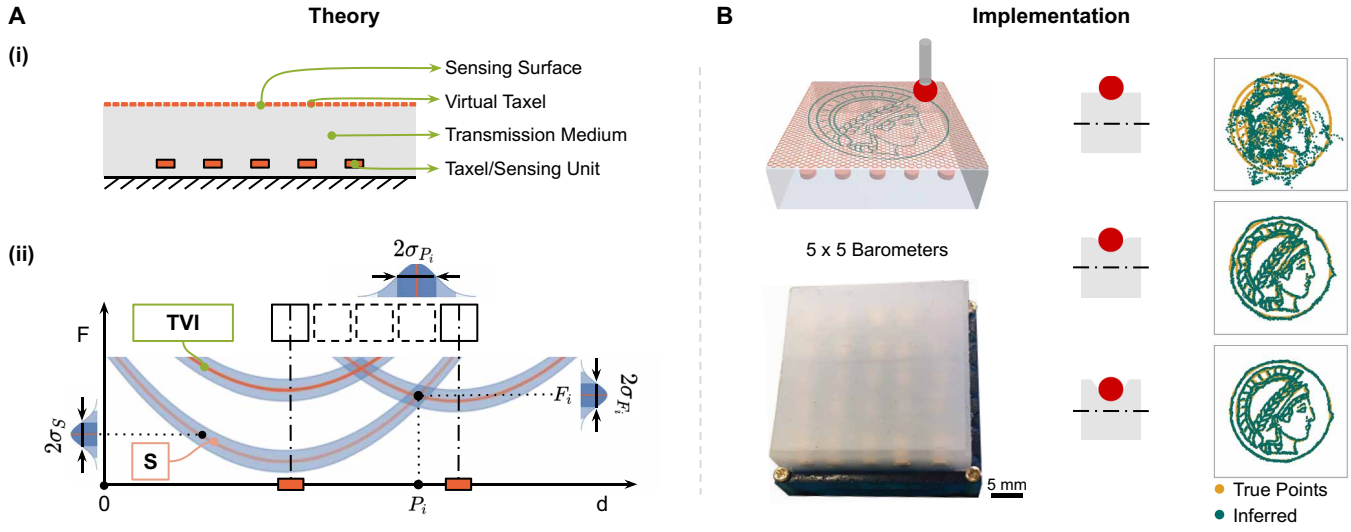

Fig. 1. Overview of the sensor design approach. Core components of the theory in (**A**) and practical implementation in (**B**). [A(i)] depicts a 1D sensor layout with sparsely placed real taxels and highly resolved virtual taxels. [A(ii)] shows the orange TVIs that are the force F needed to elicit the same taxel value S depending on the distance d from the sensor unit. The intersection of TVIs of two sensors indicates a hypothetical contact point P_i with a force strength F_i. The measurement noise σ_S in shaded blue leads to uncertainty of the position σ_{Pi} and force σ_{Fi}. More details are given in Fig. 2. (B) shows validation of our theory on a 2D sensor that embeds 25 barometers in an elastomer (EcoFlex 00-30) with a grid layout (5 by 5) to realize the SR functionality. As a demonstration, a 4-mm red spherical indenter contacts the square sensor surface (34 mm by 34 mm) following the "Minerva" pattern (diameter of 26 mm) with different depths (1.2 mm ≈ 0.2 N, 2.4 mm ≈ 0.6 N, 3.6 mm ≈ 1.0 N). The sensor can resolve the individual contact locations with high accuracy for sufficiently large indentation depths.

F and the displacement d between the contact center and the taxel center:

$$s = f(F,d) + \epsilon_S \tag{1}$$

where ϵ_S is the taxel measurement noise with a constant SD σ_S:

$$\epsilon_S \sim \mathcal{N}(0, \sigma_S^2) \tag{2}$$

To relate the sensor measurement noise ϵ_S to force values F, we assume a linear relationship. Formally, the sensor's response to an applied force at distance 0 should be $f(F,0) = 1/c \cdot F$, and to simplify the notation, we set $c = 1$. However, our analysis can be easily adapted for different values of c and for nonlinear monotonic relationships. A detailed analysis of c for the sensor type used in this article is provided in Fig. 3C(iii), fig. S5C, and supplementary section E.1, which supports our linearity assumption. One of our main contributions is to introduce the TVIs as an important characteristic function of the system.

Definition: Taxel Value Isoline (TVI) are a family of curves

$$I^S(d) = \begin{cases} F & \text{with } f(F,d) = S \\ \text{undefined} & \text{if no such } F \end{cases} \tag{3}$$

where the mean taxel output (Eq. 1) has a constant value S.

The TVIs for the model system and the effect of measurement noise are shown in Fig. 1A(ii). Intuitively, the isolines quantify how much force is needed along the surface to yield the same sensor value. To activate a taxel with a particular value, the required force strength is smaller when the contact location is closer to the taxel. On the basis of these isolines, we can derive the accuracy distributions of contact localization, force quantification, and the distribution of sensitivity over the sensing surface. Our method is based on the conditions for unique nonlinear triangulation and the geometry of intersecting isolines with their uncertainty bands, as shown in Fig. 2.

Superresolution in 1D

We are interested in knowing when a single contact point can be localized at SR, meaning much more accurately than the distance between taxels. Intuitively, this is possible when two or more taxels measure nonzero responses to the contact force and the activation pattern of the taxels is unique for this location. More formally, this condition can be analyzed with the TVIs. The minimal setting of two taxels located at a distance of D is shown in Fig. 2.

A particular contact event causes a sensor reading in both sensors S-1 and S-2. The TVI corresponding to a sensor reading of S-1 relates the position to the force of the potential contact point. Only if the TVIs from both sensors intersect can the contact position be localized, up to some uncertainty introduced by the measurement noise σ_S (Eq. 1). With this insight, we can derive the minimal force F_S (force sensitivity) that allows for SR localization, where at least two isolines intersect. We can find this minimal force, where the isoline corresponding to the smallest taxel sensitivity $S_{\min}$ intersects with TVIs from neighboring taxels. The area where $F \geq F_S$ is shaded in green in Fig. 2A(i).

As we assume an additive measurement noise, the uncertainty is also added to the isolines. We are interested in how this affects the ability to localize the contact position and to infer force magnitude. For the case of parabolic TVIs, we have to consider different possible scenarios, as shown in Fig. 2A(ii). For contact locations between the two taxels, marked with p_1, p_2, the SD for the force estimation is actually constant and given by σ_S. There is no dependency on the taxel distance D. For contact points close to the taxel and outside the taxel pair, the uncertainty of the force magnitude grows with

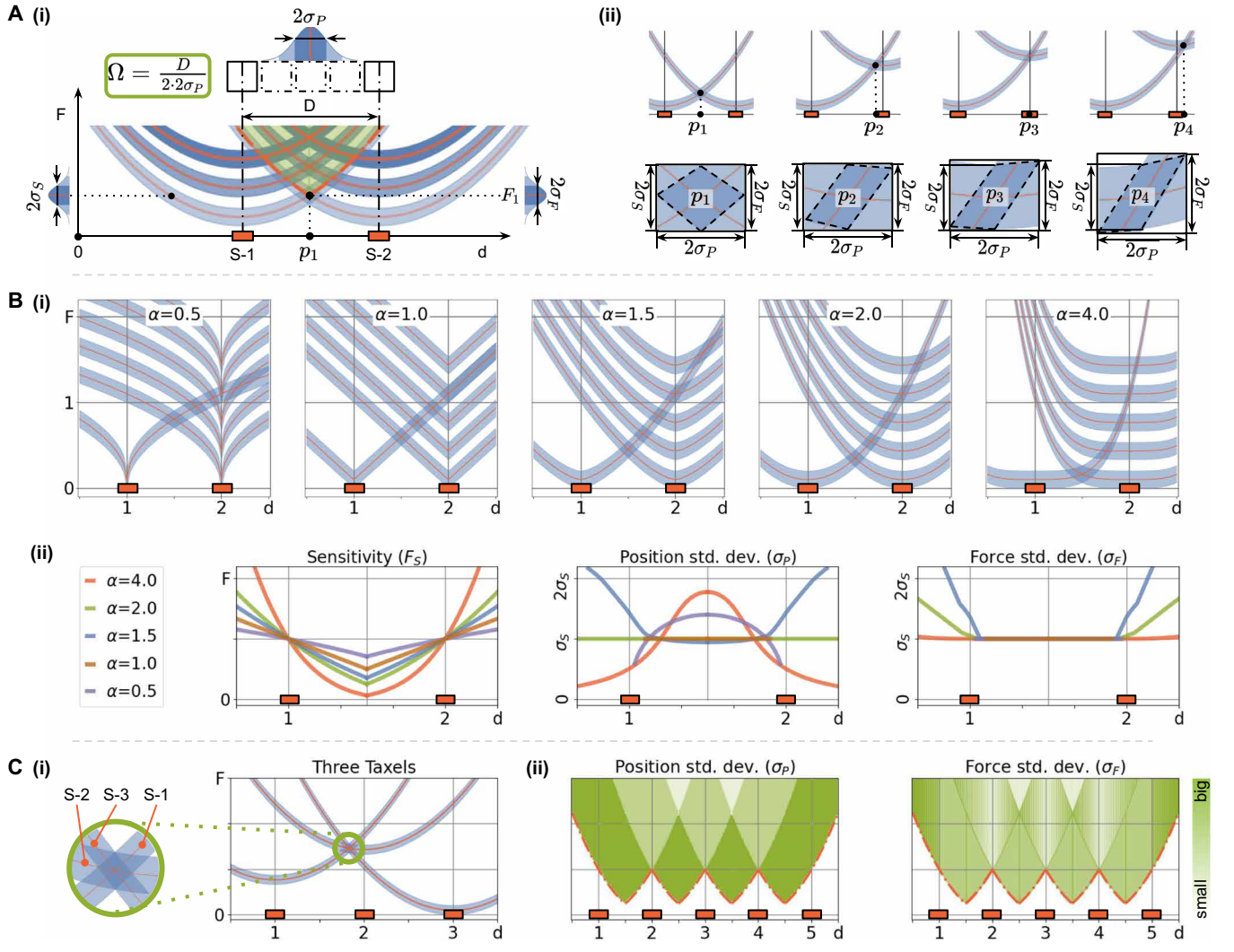

Fig. 2. Theory of superresolution sensing in 1D. (**A**) Model used for contact point localization at SR (Ω; Eq. 4). [A(i)] shows the intersection of TVIs of two sensors (marked as S-1 and S-2). The place where the lines corresponding to the particular sensor readings cross is the contact location that is marked as p_1. The measurement noise σ_S leads to uncertainty of position σ_P and force σ_F. [A(ii)] Different intersection types. (**B**) Effect of TVI shape on SR characteristics. [B(i)] TVIs are modeled as $|d|^\alpha$ + const for two taxels (at distance 1) with different attenuation exponents α. Note the different shapes of the intersection areas. [B(ii)] Resulting sensitivity (minimum force), SD of position localization, and SD of force inference. (**C**) Theoretical SR characteristics of a 1D sensor with multiple taxels. [C(i)] Three taxels localizing a single contact. Uncertainty is decreased because of averaging of independent noise sources and larger TVI slopes. [C(ii)] The spatial distribution of accuracy for a single contact. Below the orange dash-dotted line (sensitivity), no SR localization is possible. Notice the increase in accuracy for higher forces because multiple taxels are activated.

distance (p_3, p_4). The SD for position localization σ_P is typically largest in the center between the taxels and gets smaller on either side (exceptions are discussed in the following). The exact equations to compute these SDs are given in supplementary section A and visualized in Fig. 2B, as described below.

Knowing the position accuracy σ_P, we can quantify the SR capability. For simplicity, we use $2\sigma_P$ as the size of a virtual taxel, as shown in Fig. 2A(i), corresponding to a confidence interval of about 68%. Thus, the spatial resolution is $2\sigma_P$. Between two sensors at a distance D, we can distinguish $D/2\sigma_P$ virtual taxels, which we define as SR factor with respect to (w.r.t.) the number of real taxels n [$n = 2$ in Fig. 2A(i)]:

$$\Omega = \frac{D}{n \cdot 2\sigma_P} \tag{4}$$

As summarized in Table 1, another commonly used metric for the SR factor divides D by the localization prediction error [root mean square error (RMSE) or mean absolute error].

Influence of the isoline shape

The shape of the TVIs depends on the properties of the transmission medium and the sensor unit type. We study the effect of the TVI shape on the accuracy of single contact force inference. We follow the general model showing that the response of a taxel to a force on the surface decreases monotonically with distance from the taxel center. This, in turn, leads to a monotonically increasing TVI.

We assume that the attenuation of taxel response behaves as $s \propto 1/|d|^\alpha$ for a force at distance $|d|$ from the taxel center with the attenuation exponent α. Without loss of generality, we consider two taxels at a distance of 1. Their TVIs are given by

$$I_1^{S_1}(d) = g(S_1) + |d|^{\alpha} \quad (5)$$

$$I_2^{S_2}(d, s) = g(S_2) + |1 - d|^{\alpha} \quad (6)$$

where $g(S)$ is the force corresponding to the measurement at distance 0. The TVIs for different attenuation behaviors are shown in Fig. 2B. The accuracy of SR sensing is strongly affected by α. For instance, for linear attenuation ($\alpha = 1$), the localization will only be possible between the taxels, but not outside, because it results in an unbounded intersection area. For concave curves ($\alpha < 1$), there can be three intersection areas: One is between the two taxels and the other two are outside, which makes the reconstruction not unique. For the sake of comparison, we assume that, in this case, the correct intersection is known.

Smaller attenuation exponents yield a smaller sensitivity (bigger F_S) between the taxels but, in general, a more homogeneous distribution [Fig. 2B(ii)]. The position accuracy, measured by the SD, σ_P, is constant for $\alpha = 2$. For normalized TVIs, as used here for comparison, $\sigma_P = \sigma_S$. The general case is given below. For $\alpha > 2$ and $\alpha < 1$, we find a reduced position accuracy between the taxels. For $\alpha > 2$, the reduced position error at the outside is paid by an increase in minimal force (reduced force sensitivity). The ability to infer the force magnitude, given by σ_F, is constant between the two taxels, irrespective of α. For contact points outside, larger values of α are better, whereas for $\alpha \leq 1$ no detection is possible. For $1 < \alpha < 2$, the position error and force error are both high outside. From this analysis, $\alpha = 2$ yields the best overall characteristics, namely, having high force sensitivity (small F_S), high position, and force accuracy (small σ_P and σ_F, respectively). Values $\alpha > 2$ trade off some SR by sensitivity, but are generally also good. Taxel response attenuation with exponent $\alpha < 2$ should be avoided, if possible.

An approximate relationship between σ_P and σ_S for the more general TVIs $I^S(d) = g(S) + \lambda |d|^{\alpha}$ is given by

$$\sigma_P = \frac{2\sigma_S}{m_1 + m_2} \quad (7)$$

where $m_1 = \lambda\alpha |d|^{\alpha-1}$ and $m_2 = \lambda\alpha |D - d|^{\alpha-1}$ are the absolute derivatives of the TVIs as detailed in supplementary section A. For simplicity, we can use the position accuracy at $d = D/2$ (which is the worst for typical exponents, $\alpha \geq 2$) for $n = 2$ sensors to quickly compute the SR factor analytically (Eq. 4):

$$\Omega = \frac{D\lambda\alpha (D/2)^{\alpha-1}}{2 \cdot 2\sigma_S} \quad (8)$$

To be more accurate, we need to consider all positions between taxels instead of the middle one, as done in Fig. 3D(i) and detailed in supplementary section E.1.

Multiple taxels in a line

A real sensor should contain more than two taxels, so let us consider multiple taxels (with quadratic isolines) equidistantly placed in the transmission medium [as shown in Fig. 1A(i)]. As expected, in the area where more than two taxels respond to the contact stimulation, higher localization accuracy is possible, as shown in Fig. 2C(i). This leads to a reduction in uncertainty about the contact force due to two effects. The first one is the averaging of independent noise sources leading to a factor of $\sqrt{1/a}$, where a is the number of active taxels. The second effect comes from the intersection of TVIs from more distant taxels, which, due to a higher TVI slope, results in a lower uncertainty as apparent from Eq. 7. The sensitivity F_S is shown in Fig. 2C(ii) as a dash-dotted lower bound, together with the accuracy of localization σ_P and force quantification σ_F. The sensitivity is not homogeneous and is higher between taxels (lower minimum force), which might be an unexpected result at first glance. In summary, the most important take-home message is to have multiple taxels responding to a contact force because it improves accuracy. Closer placement of taxels increases both sensitivity and accuracy, whereas reducing taxel measurement noise improves accuracy but not sensitivity.

Multiple contact points

In many applications, we are interested in detecting multiple simultaneous contact points. To detect two contact points, we need at first glance two pairs of taxels. However, when the contact points are too close, spurious contact points would be detected because of additional intersections of TVIs. The basic condition for successfully distinguishing them is shown in Fig. S2. There should be at least two taxels between these two contacts, and at most one taxel of them that is evoked by one contact, not the other. With higher forces applied by these two contacts, the minimal distinguishable distance for double simultaneous contacts is larger.

Physical implementation in 1D

External contact at the sensing surface causes deformation of the transmission medium (e.g., the elastomer) that can be measured by physical sensor units (taxels). On the one hand, we investigate the influences of taxel placement and transmission medium properties on the TVIs and on the sensitivity. On the other hand, we augment our theoretical analysis by measuring the response curves of three suitable real physical sensors and choose one of them to validate our proposed theory.

Physical factors of the transmission medium influencing TVIs

When designing a sensor, many decisions need to be made—for instance, choosing the optimal positions to place the sensor units within the transmission medium; deciding the structure of the transmission medium, such as its thickness; and selecting materials with suitable properties, such as the Poisson's ratio. We built a static mechanical model simulated with the finite element method (FEM) using Ansys (*50*) to investigate the factors. Details are explained in supplementary section C. Our analysis indicates that the dependency of the deformation on the depth has an effect on the TVIs and suggests placing sensors more close to the sensing surface for higher sensitivity. Considering the structure design, thicker material causes more displacement and, in turn, increases sensitivity, because the fixed boundary effect becomes less dominant. From the material property perspective, the Young's modulus and the Poisson's ratio are the two main properties of the transmission medium we consider. The Young's modulus describes how easy the material deforms and has a proportional effect on the deformation. A soft material (small Young's modulus) not only improves sensitivity but also is increasingly deformed by inertial effects (worse with increasing high density) and might not be able to withstand strong interaction forces. The Poisson's ratio measures the relative transverse/axial expansion when the material is axially compressed. Most elastomers have Poisson's ratio around 0.5, and metals have around 0.3 (*51*). Decreasing the ratio,

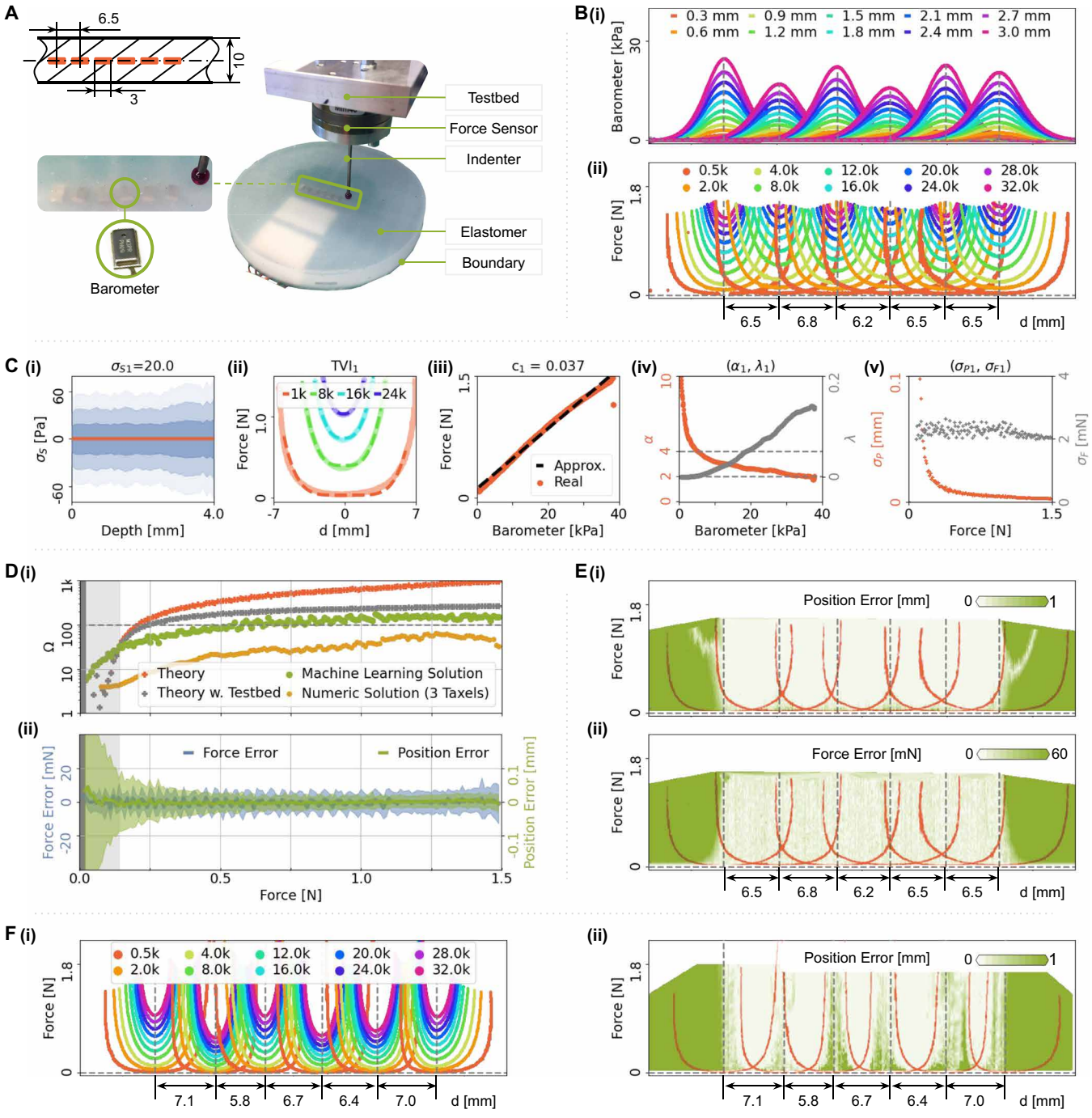

Fig. 3. Superresolution in 1D. Real line sensor device with six barometer taxels at a distance of about 6.5 mm. (**A**) Sensor device with stimulation testbed. (**B**) Taxel response for different indentation depths (i) and resulting TVIs for different sensor values (ii). (**C**) Analytical calculation based on the theory performed for one of the taxels. In (i), we assure that the sensor measurement noise is constant with $\sigma_s = 20.0$ Pa. The position and force SD (v) are analytically derived from the approximated TVIs (ii) with appropriate parameters c, α, λ (iii, iv). (**D** and **E**) Quantitative evaluation of the sensor device using ML models to infer the position and force magnitude. [D(i)] SR factor depending on the contact force magnitude as predicted by the theory without and with testbed precision, and as achieved by the ML solution and the numeric solution. [D(ii)] Position and force error of the ML solution depending on stimulation force: mean and SD over the 32.5-mm sensing surface between taxel 1 and 6. (E) Spatially resolved position error (i) and force error (ii). The orange lines are the TVIs for the smallest sensor value [500 Pa in B(ii)]. (**F**) TVIs (i) and spatially resolved position error (ii) for another 1D sensor layout with varied adjunct sensor distances.

the radial displacement becomes much less sensitive, whereas the depth displacement has higher sensitivity (lower TVIs). Thus, depending on the measurement direction of the real sensor unit, different Poisson's ratios are preferred.

Influences of the indenter geometry on the TVIs

In real applications, the sensing devices will certainly touch objects of different shapes and sizes. To study the effect on the sensing performance, we simulate the displacement caused by three different indenter shapes: a sphere, an ellipsoid, and a cylinder. We find that the shape has only a small influence on the TVIs, and flatter indenters cause decreased displacement near the center and yield flatter TVIs, as visible in Fig. S3B(iv). A similar effect appears when increasing the indenter size. Also, the sensitivity to shear forces is reduced. For small forces, where only two TVIs intersect, we can conclude that the localization performance decreases. However, for larger forces, this might be counteracted by more taxels being activated, which we will investigate in a future study. In summary, sensors can achieve higher localization performance and sensitivity for smaller contact surfaces.

TVIs of real sensors

We consider strain gauges that measure the change in curvature along one direction averaged over the sensing area (*31*, *32*), accelerometers that are able to measure the absolute inclination of the local elastomer patch using the gravity direction as a reference (*52*), and barometers that sense the volume change caused by the material's deformation in the form of isotropic pressure (*48*, *53*). As detailed in supplementary section D, the strain gauge has a nonmonotonic behavior where one strain gauge value has several position-force possibilities. The accelerometer does not have this problem but has a tiny "blind spot" directly above the sensor unit (no inclination); however, SR localization is well possible. The barometer shows the convex and monotonic properties, as described in our proposed theory.

Theoretical prediction

Because of the convexity and symmetry of the barometer's isolines, we use it to validate our proposed theory. We mold six barometers in the elastomer along a straight line with approximately 6.5-mm distance to each other as shown in Fig. 3A. The testbed carries a 4-mm spherical indenter and contacts the surface along the sensor placement center line. Sensor values, force values, and indentation positions and depths are recorded at 5001 positions evenly along the line (50 mm in total, 0.01 mm sample interval) with 40 incremental indentation depths (0.1 mm each) at each position. The resulting taxel responses and the TVIs are presented in Fig. 3B. They suggest a very good SR potential.

The measurement noise (σ_S) of the barometer sensors is almost invariant to the indentation depth [see Fig. 3C(i)]. Following our theory, the sensor noise introduces uncertainties in the position and force strength inference (σ_P and σ_F) as detailed above. We fit the parametric isolines $I^S(d) = cS + \lambda|d|^\alpha$ to the data [Fig. 3C(ii)] and acquire the constant c [Fig. 3C(iii)], attenuation coefficient λ, and power α [Fig. 3C(iv)]. Here, we find that the attenuation power α depends strongly on the barometer value. For small values (small forces), α is about equal to 10, whereas for larger values α is about 2. The effect of this nonlinearity on the localization accuracy (σ_P) is visible in Fig. 2B(ii). As shown in Fig. 3C(v), placing two identical taxels at a distance of 6.5 mm and using Eq. 7 result in force-dependent uncertainties. The uncertainty about the force magnitude σ_F is relatively constant, whereas the localization uncertainty σ_P decreases markedly with increasing contact force. In addition to the excitation of more taxels, this is a further reason for low prediction errors at higher contact forces.

The theoretical SR factor for our line sensor (six taxels over a 32.5 mm distance) is calculated by

$$\Omega_i = \frac{32.5}{6 \cdot 2\sigma_{P_i}} \tag{9}$$

where i indicates which sensor is used. The red dots in Fig. 3D(i) show the averaged Ω over six sensors with respect to the contact force strength. The testbed has a position resolution of 0.0075 mm that introduces additional uncertainty in contact localization (added to σ_{P_i} in Eq. 9), resulting in values shown as gray dots in Fig. 3D(i). These two SR factors can be taken as upper baselines to evaluate the signal processing methods. Detailed information on the calculations can be found in supplementary section E.1.

Practical force inference

To solve the inverse problem of predicting the indentation position from the sensor measurements, we compare two methods. We first consider a numerical solution by taking three sensors with the highest sensor values among six, looking for the intersection points ($P_{1,2}$, $P_{2,3}$, and $P_{1,3}$) of the TVIs, and averaging them to get the contact location (see supplementary section E.2). The second and preferred method for data processing is instead a neural network regression model (MLP structure) using squared error loss, which yields a prediction with minimal variance. In this way, we circumvent a manual computation of intersection locations, which suffers from inaccuracies due to real-world deviations from the idealized TVIs. For the architecture and training details, see supplementary section E.3. The results are summarized in Fig. 3 (D and E). We take the RMSE as σ_P to calculate the SR factor (Eq. 4), shown as yellow dots for the numerical solution and green dots for the ML solution in Fig. 3D(i). The inference accuracy of the position is higher with stronger indentation forces. The ML solution approaches the theoretical prediction (including the testbed errors) and outperforms the numerical solution (three taxels). As expected, the theoretical predictions are higher, because they represent the best achievable results. The ML solution nevertheless excels the theory in the low force operation range (0.02 to 0.14 N). An explanation is that, in this region, the force is below the minimal force (sensitivity) for many contact locations [1 kPa shown in Figs. 2C(ii) and 3C(ii)] where our theory does not make predictions because no TVI intersections are available. The ML solution can still predict the taxel center in these cases. Numeric values for localization errors of all methods are provided in Table 2.

We use two neural network regression models to predict the contact location and force magnitude, respectively (details in supplementary section E.3). The inference accuracy of the position is higher with stronger indentation force and slightly lower for force magnitude, but generally very accurate (evaluated at locations that were not included during training), as shown in Fig. 3D(ii). Averaging it over the applied force range (from 0.02 N to 1.5 N), we obtain an average SR factor of 106 with the ML method, compared to the prediction of 187 from the theory with testbed consideration.

The spatial distribution of position error and force magnitude error of the prediction models are shown in Fig. 3E. To show the

Table 2. The RMSE of contact localization (mm) w.r.t. the indentation force. In 1D, we compare the theoretical predictions with the ML approach and our numerical computation. For the 2D case, we report, in addition to the used MLP method, a version with separate prediction for *x* and *y* component with increased performance.

Force interval (N)	0.02–0.14	0.14–0.2	0.2–0.4	0.4–0.6	0.6–0.9	0.9–1.2	1.2–1.5	Overall
1D theory	0.714	0.052	0.017	0.008	0.005	0.004	0.003	0.053
1D theory + testbed	0.721	0.060	0.024	0.016	0.013	0.012	0.011	0.060
1D ML	0.196	0.079	0.051	0.032	0.024	0.019	0.018	0.042
1D numeric (3 taxels)	0.668	0.517	0.264	0.134	0.098	0.068	0.049	0.158
1D numeric (2 taxels)	1.074	0.678	0.476	0.203	0.129	0.103	0.071	0.244
2D ML	0.567	0.230	0.158	0.120	0.107	0.107	0.120	0.161
2D ML (separate *x*, *y*)	0.485	0.219	0.139	0.101	0.086	0.082	0.082	0.132

effect of different overlappings of the TVIs, we present in Fig. 3F(i) a sensor with varying distances between the sensor units. The position errors [Fig. 3F(ii)] increase between taxels with larger distances. In both cases, the overall shape resembles our theoretical prediction; compare with Fig. 2: Higher errors occur in locations where fewer TVIs overlap. Note that this is not a problem of lacking data, because we record plenty of data also in these regions.

Our analysis uses data with a very fine spacing of contact locations (every 0.01 mm). It would be interesting to know how much data are really required. We investigate the performance of the ML inference method depending on the spacing of training contact points and present the result in fig. S6B. Already with a contact interval of 0.5 mm, a localization accuracy below 0.1 mm is achieved (evaluated on unseen contact locations at 0.01-mm resolution in a force range of 0.02 to 1.5 N). For comparison, we also consider a simple *k*-nearest neighbors (kNNs) method, mimicking a lookup table. For coarse data, the kNN falls short, but for data finer than 0.04 mm resolution, both methods perform similarly.

Superresolution in 2D

The above analysis for the 1D case helps us to investigate a sensor with a flat or curved 2D sensing surface. To simplify the analysis, we continue to assume a homogeneous transmission medium and an isotropic sensor unit, which is, for instance, approximately true for barometric sensors but violated for strain gauge sensors. We consider a flat 2D sensing surface with coordinates *x* and *y*. The concept of isolines translates into isosurfaces, as shown in Fig. 4A(i). However, we still call them TVIs for consistency. With only two taxels, an accurate localization can only be done along one dimension (*x*), but not along two (*x* and *y*), as shown in Fig. 4A(ii). To make proper SR localization possible, at least three taxels need to respond to a stimulus, as shown in Fig. 4A(iii). As before, the accuracy increases if more taxels are involved, and the sensitivity is higher between taxels over the sensing surface [Fig. 4A(iii)]. As detailed in supplementary section F, to localize two simultaneous contacts, at least six taxels are required to respond. Similar to the 1D case, if the contacts are too close, spurious intersections can occur. The spurious intersections can be ruled out because of high elongation in one direction, similar to Fig. 4A(ii). This is a new feature that was not observed in 1D. Very similar considerations are also valid for curved sensing surfaces, which is illustrated in Fig. S7C(iv).

We mold 25 barometers, as shown in Fig. 4B(i), in the elastomer with a 5-by-5 grid layout and about 6.5 mm of distance to each other, as suggested by the isoline shape and the 1D experiments. A testbed carries a 4-mm spherical indenter and contacts the surface at given locations, as in the 1D case Fig. 3A. Sensor values, force values, and indentation positions and depths are recorded at 69 by 69 positions (a grid with 0.5 mm apart from each other) evenly distributed on the sensing surface (34 mm by 34 mm) with 20 incremental indentation depths (0.2 mm each) at each position. The resulting taxel responses are presented in Fig. S8.

We use two neural network regression models (MLP architecture) to predict the indentation position and force magnitude, respectively. The architecture and training details are provided in supplementary section F. The results are summarized in Fig. 4 (C and D). Figure 4C(i) shows the averaged SR factor Ω of 1260 using

$$\Omega_k = \frac{A}{n \cdot \pi \cdot \mathrm{RMSE}_{x,k} \cdot \mathrm{RMSE}_{y,k}} = \frac{26 \cdot 26}{25 \cdot \pi \cdot \mathrm{RMSE}_{x,k} \cdot \mathrm{RMSE}_{y,k}} \quad (10)$$

where *A* is the sensing area and *k* is the *k*th force interval (0.01 N) over a force range of 0.02 to 1.5 N. The inference accuracy of the position is higher with stronger indentation force, as shown in Fig. 4C(ii). The force accuracy is relatively constant, with 0.01 N (RMSE) on average. The averaged error of inferred locations is at 0.161 mm (RMSE), and for forces larger than 0.2 N, an error of 0.120 mm (RMSE) is achieved. The spatial distribution of position and force magnitude error for different indentation depths are shown in Fig. 4D. With increased indentation depth, the position accuracy improves. In coherence with our theory, the improvement is smaller at the boundaries because less TVIs overlap. In comparison, the spatial distribution of the force error is relatively homogeneous. The error increases slightly with increased indentation depth, and forces at the boundaries tend to be slightly underestimated. The performance can still be improved by training MLP models for *x* and *y* separately (see Table 2). Details can be found in Materials and Methods.

DISCUSSION

We present an approach to characterize, analyze, and predict force sensation at SR for tactile sensors. Our theory is based on sensor isolines that allow for a direct assessment of the uniqueness of contact position reconstruction. We derive quantities such as minimum force sensitivity, localization, and force sensing accuracy. These allow us to analytically compute the SR factor, namely, the number of distinguishable locations between two real sensor units.

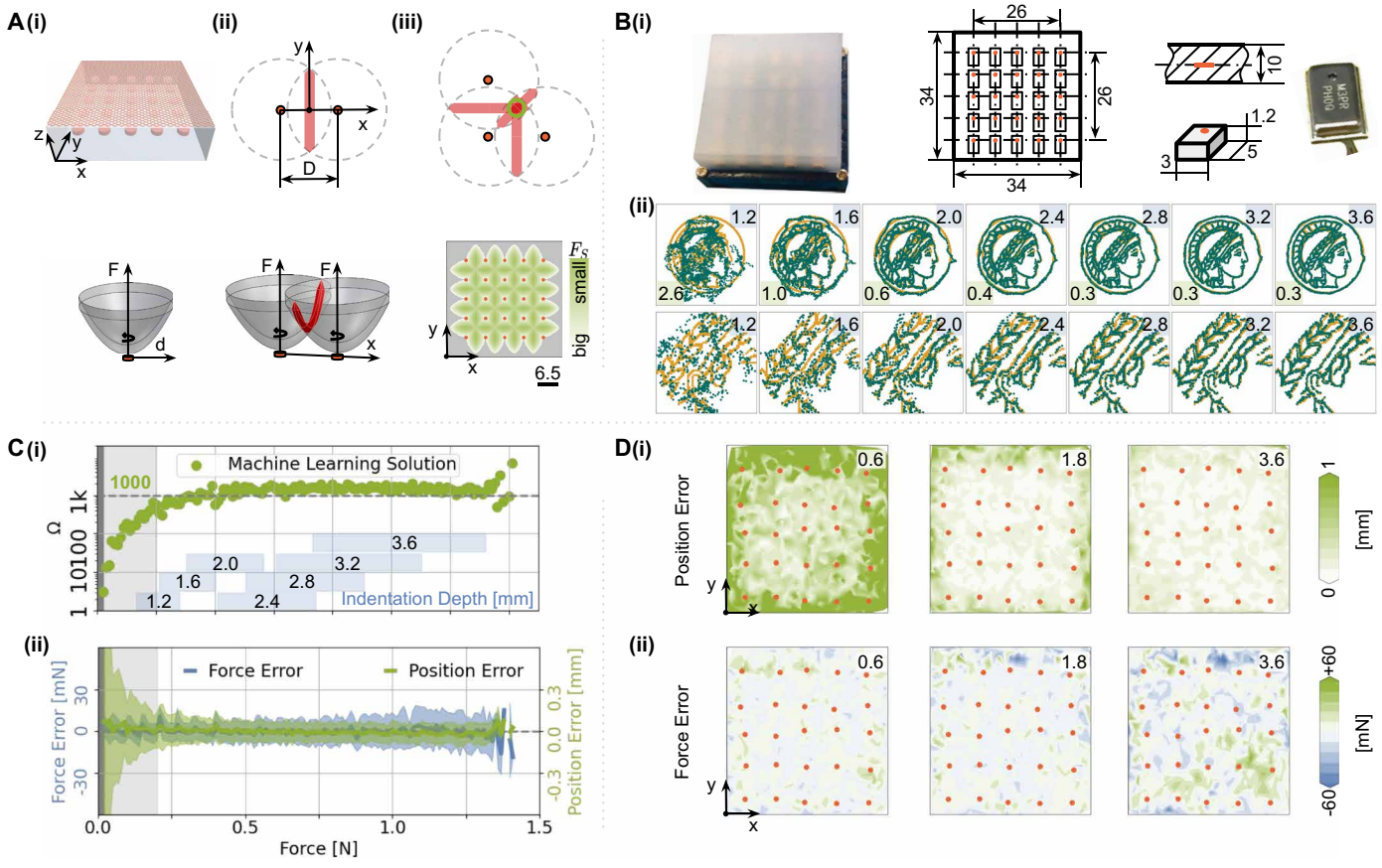

Fig. 4. Superresolution in 2D. (**A**) 2D sensor arrangement and taxel value isolines for a 2D sensing surface. [A(i)] Bottom: TVI (iso-surface) for a single taxel. [A(ii)] Intersection volume (due to measurement uncertainty) for two taxels at a distance *D* along the *x* axis; see top view. The localization would be very uncertain along the *y* direction. [A(iii)] Proper localization requires at least three taxels for one contact point. The lower part shows a grid sensor arrangement with resulting sensitivity over the surface. Locations between taxels are more sensitive, requiring a smaller force (F_S) to activate them. (**B**) presents our custom 2D sensor designed according to our theory guidelines. [B(i)] is a picture of the sensor together with its geometric properties in a millimeter (mm) scale. [B(ii)] shows a performance illustration for the SR functionality. A 4-mm spherical indenter contacts the surface following a circular "Minerva" pattern (yellow) with different indentation depths (stated in the upper right corner), and a trained ML model infers contact locations (green), with RMSE (mm) indicated in the bottom left corner. The lower row shows a detailed view of the central region. (**C** and **D**) Quantitative evaluation of the sensor device using ML models to infer the position and force magnitude. [C(i)] SR factor depending on contact force magnitudes over the sensor's center region (26 mm by 26 mm). [C(ii)] Position and force errors depending on stimulation forces: mean and SD. (D) Spatially resolved position error (i) and force error (ii) with respect to indentation depths.

With the help of an FEM model, we provide guidelines for common design choices, such as placement of the sensor units within the elastomer as well as material properties. We analyze three commonly used sensor types: strain gauges, accelerometers, and barometers. Both accelerometers and barometers show the necessary properties for SR sensation within our framework. We conduct two case studies to evaluate our theory using a line (1D) and a grid (2D) of barometer sensor units embedded in elastomer skin. After our theory-informed design choices, the 1D sensor has a theoretically predicted SR factor of 187. Using ML as a practical implementation achieves a performance of 106-fold SR. Our 2D sensor with a 26 mm by 26 mm sensing surface reaches a 1260-fold SR and can localize contacts up to 0.161 mm on average.

We hope that our approach can help the design of new and capable tactile sensors. The insights from our study on soft material properties and sensing method can be summarized as follows. The sensor units in the transmission medium (elastomer) should have convex isolines. It is beneficial to have the sensor units "float" in the center of the elastomer or closer to the sensing surface. Flexible wiring helps to have the best sensitivity. A thicker elastomer layer seems beneficial, and materials with small Young's modulus, high Poisson's ratio, and big yield strength are recommended. The distance between sensor units should be such that for most of the forces, the isolines of neighboring taxels intersect. For inferring simultaneous contacts, a single sensor unit should be only activated by a single contact, and the distinguishable distance increases when the force magnitudes of multiple contacts are higher.

The decisive quantity in our theory for SR perception is spatial distribution of the uncertainty of contact location and force magnitude inference. This uncertainty can be decreased by averaging subsequent samples from the sensors (thus increasing the response time) and by moving the taxels closer together to excite more than two taxels per contact. In a practical implementation, we need a mechanism to perform the actual tactile information inference. This can be implemented numerically and using ML, where the latter shows a three times better performance. It is important to understand the

connection between the ML model and theory. Exploiting the equivalence of minimizing model uncertainty by maximum likelihood estimation and least-squares error minimization for Gaussian residuals, the ML model directly optimizes for the quantities of interest: the prediction uncertainties. Whereas the theory describes an upper limit for the SR capabilities under the model assumptions, we find that the ML methods approach the predicted accuracy in the considered real-world sensors. In this way, our theory offers guidelines toward the system-level design of ML-driven tactile sensors.

Besides the abovementioned mechanoelectrical properties, the predictions by the theory can be used to validate the suitability of the used ML model, the data collection, and the training procedure, as we can expect performances to come close to the predicted ones. We show how the inaccuracies in the testbed need to be taken into account and how much data are effectively required for good performance.

Our work enables engineers to make more informed decisions when aiming for high-resolution tactile sensing. Alternative designs can be invented that create more robust and cheaper sensors without sacrificing the required precision. The principles used in this article are applicable to a larger range of sensing mechanisms. Optimizing a design for accelerometers or Hall effect sensors might be a promising next step. We hope our work delivers an important stepping stone to ubiquitous tactile sensing in robotics. We provide further evidence that ML methods are a flexible way of performing data processing in tactile sensing. They are capable of approaching the theoretical limit in terms of superresolution sensing, provided a sufficient amount of high-quality data is available. Promising directions for future research include the extension of our work to shear forces and the investigation of structured transmission media, e.g., with ridges (*54*) or multiple layers (*18*).

MATERIALS AND METHODS

We conducted several experiments to make informed design choices and validate the proposed theory.

Finite element analysis

To analyze the physical factors of the transmission medium influencing TVIs, we built a suitable finite-element model using Ansys (*50*). The model includes suitable default values of Young's modulus and Poisson's ratio for the material of EcoFlex 00-30 (70 kPa, 0.4999). Details of the modeling can be found in supplementary section C.

Sensor

We designed two sensors (1D and 2D) to validate the proposed theory. The 1D sensor embeds six barometric units (MPL3115A2) along a line (6.5-mm spacing) inside an elastomer (diameter: 120 mm; thickness: 10 mm), and the 2D sensor comprises 25 barometric units with a 5-by-5 grid layout (6.5 mm spacing) inside an elastomer (dimensions: 34 mm by 34 mm; thickness: 10 mm). We soldered extra thin wires (Cu-enameled wire with a diameter of 0.15 mm; ME-Meß Systeme GmbH) to the units to be able to model them inside the elastomer (EcoFlex 00-30) with minimal mechanical influence of the taxel. We designed molds for the sensor spacing and the elastomer molding procedure. The molds were 3D-printed (3D printer: Formlabs Form 3, Material: Tough). We molded these barometric units floating in the middle of the elastomer. The sensor values of the barometric units (MPL3115A2) were acquired through the evaluation board supplied by Adafruit with additional 16-channeled analog multiplexers (CD74HC4067), and all of them were delivered to a laptop (ThinkPad L570) through Arduino Mega 2560.

Testbed

We created a custom testbed with three degrees of freedom (DoFs). Three DoFs control the Cartesian movement of the probe using linear guide rails (Barch Motion) with a precision of 0.0075 mm. The movement of the linear rails for one rotation of the step motor (57CM23) is 75 mm. The step motor is driven by the driver (Leadshine DM542S) with a stepper resolution of 10,000 steps per revolution. The 4 mm spherical probe is fabricated from an aluminum alloy and is rigidly attached to the Cartesian gantry via an ATI Mini40 force/torque sensor with a force resolution of 0.01/0.01/0.02 N ($F_x/F_y/F_z$). The sensor is positioned on the base, and the indenter is used to contact it at the desired location.

Data

To obtain a variety of normal forces, the indenter was moved to a specified location, touched the sensing surface, and deformed it increasingly by moving normal to the surface with a fixed incremental step. After a pause of 2 s to allow transients to dissipate, we simultaneously recorded the contact location, the indenter contact force from the testbed's force sensor, and the barometric units' values from the molded sensors. All the data were collected and combined using a standard laptop. More specifically, for the 1D sensor (Fig. 3), the testbed made the indenter contact 5001 positions evenly spread along the sensor center line (from −25 to 25 mm) with 40 incremental indentation depths (0.1 mm each) at each position. For the 2D sensor (Fig. 4), 69-by-69 positions (a grid with 0.5 mm apart from each other) evenly distributed on the sensing surface (34 mm by 34 mm) were probed by the indenter with 20 incremental indentation depths (0.2 mm each). The data of the "Minerva" pattern (diameter: 26 mm) were collected similarly for validating the SR functionality. The pattern has a position resolution of 0.0074 mm. The indenter probed the sensor at each position (rounded by the testbed resolution of 0.0075 mm) with 10 incremental steps (0.4 mm each with a transients pause of 2 s).

TVIs and related parameters

We implemented the following steps to compute the isolines (Fig. 3 and Fig. S4). First, we linearly interpolated the sensor values and force values. Second, we chose a position-related sensor value and found the corresponding force measurement in that position. Third, we drew the position-force curve for that sensor value with the same color as shown in Fig. 3 (B and F). On the basis of the derived isolines, we used curve function ($\lambda \cdot d^{\alpha} + g(S)$) to fit each derived isoline Fig. 3C (ii and iv). The constant c was calculated by dividing $g(S)$ by S at distance 0 [Fig. 3C(iii)]. The theoretically achievable σ_P and σ_F can be calculated using Eq. 7 [Fig. 3C(v)].

Machine learning

For the 1D sensor, we used a standard MLP with six fully connected hidden layers with 100 rectified linear units each. The data consisted of 132,000 samples that were split into datasets of training, validation, and test with a ratio of 3:1:1. The data were recorded in the region from the center of the left barometric unit to the right one (32.5 mm in total, contact location interval of 0.01 mm). The models were

trained with the mean-squared error loss, the Adam optimizer (learning rate: 5×10^{-4}, epsilon: 10^{-5}), and a mini-batch size of 200 samples in 1 million iterations. The models for position and force inferences were separately trained using the same architecture and training settings. For the 2D sensor, the setting was the same as above, except that we have only 95,000 data points (contact location interval of 0.5 mm), use 10 layers, choose a learning rate of 2×10^{-4}, and have a mini-batch size of 100.

SUPPLEMENTARY MATERIALS

www.science.org/doi/10.1126/scirobotics.abm0608
Sections A to F
Figs. S1 to S8

REFERENCES AND NOTES

1. J. C. Yang, J. Mun, S. Y. Kwon, S. Park, Z. Bao, S. Park, Electronic skin: Recent progress and future prospects for skin-attachable devices for health monitoring, robotics, and prosthetics. *Adv. Mater.* **31**, 1904765 (2019).
2. Q. Li, O. Kroemer, Z. Su, F. F. Veiga, M. Kaboli, H. J. Ritter, A review of tactile information: Perception and action through touch. *IEEE Trans. Robot.* **36**, 1619–1634 (2020).
3. M. L. Hammock, A. Chortos, B. C.-K. Tee, J. B.-H. Tok, Z. Bao, 25th anniversary article: The evolution of electronic skin (E-Skin): A brief history, design considerations, and recent progress. *Adv. Mater.* **25**, 5997–6038 (2013).
4. R. S. Dahiya, G. Metta, M. Valle, G. Sandini, Tactile sensing—From humans to humanoids. *IEEE Trans. Robot.* **26**, 1–20 (2010).
5. K. Chin, T. Hellebrekers, C. Majidi, Machine learning for soft robotic sensing and control. *Adv. Intell. Syst.* **2**, 1900171 (2020).
6. Z. Kappassov, J.-A. Corrales, V. Perdereau, Tactile sensing in dexterous robot hands—Review. *Rob. Auton. Syst.* **74**, 195–220 (2015).
7. M. T. Francomano, D. Accoto, E. Guglielmelli, Artificial sense of slip—A review. *IEEE Sens. J.* **13**, 2489–2498 (2013).
8. R. S. Dahiya, P. Mittendorfer, M. Valle, G. Cheng, V. J. Lumelsky, Directions toward effective utilization of tactile skin: A review. *IEEE Sens. J.* **13**, 4121–4138 (2013).
9. R. Balasubramanian, V. J. Santos, *The Human Hand as an Inspiration for Robot Hand Development* (Springer Publishing Company, Incorporated, 2014).
10. E. Cheung, V. J. Lumelsky, Proximity sensing in robot manipulator motion planning: System and implementation issues. *IEEE Trans. Rob. Autom.* **5**, 740–751 (1989).
11. D. Um, B. Stankovic, K. Giles, T. Hammond, V. Lumelsky, A modularized sensitive skin for motion planning in uncertain environments, in *Proceedings of the IEEE International Conference on Robotics and Automation (ICRA)* (IEEE, 1998), pp. 7–12, vol.1.
12. W. Taube Navaraj, C. García Nuñez, D. Shakthivel, V. Vinciguerra, F. Labeau, D. H. Gregory, R. Dahiya, Nanowire FET based neural element for robotic tactile sensing skin. *Front. Neurosci.* **11**, 501 (2017).
13. C. Bartolozzi, L. Natale, F. Nori, G. Metta, Robots with a sense of touch. *Nat. Mater.* **15**, 921–925 (2016).
14. M. Chen, W. Luo, Z. Xu, X. Zhang, B. Xie, G. Wang, M. Han, An ultrahigh resolution pressure sensor based on percolative metal nanoparticle arrays. *Nat. Commun.* **10**, 4024 (2019).
15. T. Taunyazov, W. Sng, H. H. See, B. Lim, J. Kuan, A. F. Ansari, B. C. K. Tee, H. Soh, Event-driven visual-tactile sensing and learning for robots, in *Proceedings of Robotics: Science and Systems (RSS)* (2020).
16. P. Mittendorfer, G. Cheng, Humanoid multimodal tactile-sensing modules. *IEEE Trans. Robot.* **27**, 401–410 (2011).
17. J. Rogelio Guadarrama-Olvera, F. Bergner, E. Dean, G. Cheng, Enhancing biped locomotion on unknown terrain using tactile feedback, in *Proceedings of the IEEE International Conference on Humanoid Robots (Humanoids)* (IEEE, 2018), pp. 1–9.
18. C. M. Boutry, M. Negre, M. Jorda, O. Vardoulis, A. Chortos, O. Khatib, Z. Bao, A hierarchically patterned, bioinspired e-skin able to detect the direction of applied pressure for robotics. *Sci. Robot.* **3**, eaau6914 (2018).
19. P. Piacenza, K. Behrman, B. Schifferer, I. Kymissis, M. Ciocarlie, A sensorized multicurved robot finger with data-driven touch sensing via overlapping light signals. *IEEE ASME Trans. Mechatron.* **25**, 2416–2427 (2020).
20. H. Bai, S. Li, J. Barreiros, Y. Tu, C. R. Pollock, R. F. Shepherd, Stretchable distributed fiber-optic sensors. *Science* **370**, 848–852 (2020).
21. J. Park, M. Kim, Y. Lee, H. S. Lee, H. Ko, Fingertip skin–inspired microstructured ferroelectric skins discriminate static/dynamic pressure and temperature stimuli. *Sci. Adv.* **1**, e1500661 (2015).
22. Y.-C. Lai, Y.-C. Hsiao, H.-M. Wu, Z. L. Wang, Waterproof fabric-based multifunctional triboelectric nanogenerator for universally harvesting energy from raindrops, wind, and human motions and as self-powered sensors. *Adv. Sci.* **6**, 1801883 (2019).
23. W. Yuan, S. Dong, E. H. Adelson, GelSight: High-resolution robot tactile sensors for estimating geometry and force. *Sensors* **17**, 2762 (2017).
24. C. Sferrazza, R. D'Andrea, Design, motivation and evaluation of a full-resolution optical tactile sensor. *Sensors* **19**, 928 (2019).
25. L. Van Duong, R. Asahina, J. Wang, V. A. Ho, Development of a vision-based soft tactile muscularis, in *Proceedings of the IEEE International Conference on Soft Robotics (RoboSoft)* (IEEE, 2019), pp. 343–348.
26. B. Ward-Cherrier, N. Pestell, L. Cramphorn, B. Winstone, M. E. Giannaccini, J. Rossiter, N. F. Lepora, The TacTip family: Soft optical tactile sensors with 3D-printed biomimetic morphologies. *Soft Robot.* **5**, 216–227 (2018).
27. B. Lee, J.-Y. Oh, H. Cho, C. W. Joo, H. Yoon, S. Jeong, E. Oh, J. Byun, H. Kim, S. Lee, J. Seo, C. W. Park, S. Choi, N.-M. Park, S.-Y. Kang, C.-S. Hwang, S.-D. Ahn, J.-I. Lee, Y. Hong, Ultraflexible and transparent electroluminescent skin for real-time and super-resolution imaging of pressure distribution. *Nat. Commun.* **11**, 663 (2020).
28. H. Sun, K. J. Kuchenbecker, G. Martius, A soft thumb-sized vision-based sensor with accurate all-round force perception. arXiv:2111.05934 [cs.RO] (10 November 2021).
29. J. A. Fishel, G. E. Loeb, Sensing tactile microvibrations with the BioTac—Comparison with human sensitivity, in *Proceedings of the IEEE RAS & EMBS International Conference on Biomedical Robotics and Biomechatronics (BioRob)* (IEEE, 2012), pp. 1122–1127.
30. N. F. Lepora, U. Martinez-Hernandez, M. Evans, L. Natale, G. Metta, T. J. Prescott, Tactile superresolution and biomimetic hyperacuity. *IEEE Trans. Robot.* **31**, 605–618 (2015).
31. H. Sun, G. Martius, Robust affordable 3D haptic sensation via learning deformation patterns, in *Proceedings of the IEEE-RAS 18th International Conference on Humanoid Robots (Humanoids)* (IEEE, 2018), pp. 846–853.
32. H. Sun, G. Martius, Machine learning for haptics: Inferring multi-contact stimulation from sparse sensor configuration. *Front. Neurorobot.* **13**, 51 (2019).
33. H. Lee, D. Kwon, H. Cho, I. Park, J. Kim, Soft nanocomposite based multi-point, multi-directional strain mapping sensor using anisotropic electrical impedance tomography. *Sci. Rep.* **7**, 39837 (2017).
34. H. Lee, H. Park, G. Serhat, H. Sun, K. J. Kuchenbecker, Calibrating a soft ERT-based tactile sensor with a multiphysics model and sim-to-real transfer learning, in *Proceedings of the IEEE International Conference on Robotics and Automation (ICRA)* (IEEE, 2020), pp. 1632–1638.
35. Y. Yan, Z. Hu, Z. Yang, W. Yuan, C. Song, J. Pan, Y. Shen, Soft magnetic skin for super-resolution tactile sensing with force self-decoupling. *Sci. Robot.* **6**, eabc8801 (2021).
36. A. Krause, A. Singh, C. Guestrin, Near-optimal sensor placements in Gaussian processes: Theory, efficient algorithms and empirical studies. *J. Mach. Learn. Res.* **9**, 235–284 (2008).
37. G. Westheimer, Optical superresolution and visual hyperacuity. *Prog. Retin. Eye Res.* **31**, 467–480 (2012).
38. L. Liu, S. M. Kuo, M. Zhou, Virtual sensing techniques and their applications, in *Proceedings of the IEEE International Conference on Networking, Sensing and Control* (IEEE, 2009), pp. 31–36.
39. R. Mahmood, S. Jia, W. Zhu, Analysis of climate variability, trends, and prediction in the most active parts of the Lake Chad basin, Africa. *Sci. Rep.* **9**, 6317 (2019).
40. E. B. Fox, J. W. Fisher, A. S. Willsky, Detection and localization of material releases with sparse sensor configurations. *IEEE Trans. Signal Process.* **55**, 1886–1898 (2007).
41. K. S. Eu, K. M. Yap, Chemical plume tracing: A three-dimensional technique for quadrotors by considering the altitude control of the robot in the casting stage. *Int. J. Adv. Robot. Syst.* **15**, 1729881418755877 (2018).
42. V. Marx, Is super-resolution microscopy right for you? *Nat. Methods* **10**, 1157–1163 (2013).
43. Z. Zalevsky, D. Mendlovic, *Optical Superresolution* (Springer New York, 2004).
44. H. Strasburger, J. Huber, D. Rose, Ewald Hering's (1899) on the limits of visual acuity: A translation and commentary: With a supplement on Alfred Volkmann's (1863) physiological investigations in the field of optics. *Iperception* **9**, 2041669518763675 (2018).
45. G. Westheimer, S. P. McKee, Spatial configurations for visual hyperacuity. *Vision Res.* **17**, 941–947 (1977).
46. N. F. Lepora, B. Ward-Cherrier, Superresolution with an optical tactile sensor, in *Proceedings of the IEEE/RSJ International Conference on Intelligent Robots and Systems (IROS)* (IEEE, 2015), pp. 2686–2691.
47. P. Piacenza, S. Sherman, M. Ciocarlie, Data-driven super-resolution on a tactile dome. *IEEE Robot. Autom. Lett.* **3**, 1434–1441 (2018).
48. RightHand Robotics, TakkTile Kit (2021); www.labs.righthandrobotics.com/takktile-sensors.
49. T. Hellebrekers, N. Chang, K. Chin, M. J. Ford, O. Kroemer, C. Majidi, Soft magnetic tactile skin for continuous force and location estimation using neural networks. *IEEE Robot. Autom. Lett.* **5**, 3892–3898 (2020).
50. Ansys, Academic Research Mechanical, Release 18.1 (2020); www.ansys.com.

51. P. H. Mott, C. M. Roland, Limits to Poisson's ratio in isotropic materials—General result for arbitrary deformation. *Phys. Scr.* **87**, 055404 (2013).
52. P. Dallaire, P. Giguère, D. Émond, B. Chaib-draa, Autonomous tactile perception: A combined improved sensing and Bayesian nonparametric approach. *Robot. Auton. Syst.* **62**, 422–435 (2014).
53. L. U. Odhner, L. P. Jentoft, M. R. Claffee, N. Corson, Y. Tenzer, R. R. Ma, M. Buehler, R. Kohout, R. D. Howe, A. M. Dollar, A compliant, underactuated hand for robust manipulation. *Int. J. Rob. Res.* **33**, 736–752 (2014).
54. T. Q. Pham, T. Hoshi, Y. Tanaka, A. Sano, Effect of 3D microstructure of dermal papillae on SED concentration at a mechanoreceptor location. *PLOS ONE* **12**, e0189293 (2017).

Funding: We thank the China Scholarship Council (CSC) and the International Max Planck Research School for Intelligent Systems (IMPRS-IS) for supporting H.S. G.M. is a member of the Machine Learning Cluster of Excellence, funded by the Deutsche Forschungsgemeinschaft (DFG, German Research Foundation) under Germany's Excellence Strategy—EXC number 2064/1—Project number 390727645. We acknowledge the support from the German Federal Ministry of Education and Research (BMBF) through the Tübingen AI Center (FKZ: 01IS18039B).
Author contributions: H.S. and G.M. conceived the method and the experiments. H.S. drafted the manuscript. H.S. and G.M. revised it. H.S. derived the theory, designed and constructed the hardware, developed fabrication methods, designed and conducted experiments, and collected and analyzed the data. G.M. supervised the data analysis. We thank A. Levina for discussions on the analytic solution for σ_P. **Competing interests:** The authors declare that they have no competing interests. **Data and materials availability:** The data and code that support the findings of this study are available at https://dx.doi.org/10.17617/3.87.

Submitted 24 August 2021
Accepted 24 January 2022
Published 23 February 2022
10.1126/scirobotics.abm0608

Science Robotics

Guiding the design of superresolution tactile skins with taxel value isolines theory

Huanbo Sun and Georg Martius

Sci. Robot. **7** (63), eabm0608. DOI: 10.1126/scirobotics.abm0608

Science Robotics (ISSN 2470-9476) is published by the American Association for the Advancement of Science. 1200 New York Avenue NW, Washington, DC 20005. The title *Science Robotics* is a registered trademark of AAAS.